Lawrence Berkeley National Laboratory
LBL Publications

Title

Uncovering the three-dimensional structure of upconverting core—shell nanoparticles with multislice electron ptychography

Permalink

Journal

ISSN

Authors

Ribet, Stephanie M
Varnavides, Georgios
Pedroso, Cassio CS
et al.

Publication Date

DOI

Copyright Information

Uncovering the three-dimensional structure of upconverting core–shell nanoparticles with multislice electron ptychography 🗞 🄵

Stephanie M. Ribet ✉ 🄳 ; Georgios Varnavides 🄳 ; Cassio C. S. Pedroso 🄳 ; Bruce E. Cohen 🄳 ;
Peter Ercius 🄳 ; Mary C. Scott 🄳 ; Colin Ophus ✉ 🄳

Check for updates

View Online   Export Citation

Uncovering the three-dimensional structure of upconverting core–shell nanoparticles with multislice electron ptychography 🄵 🅂🄲🄸

Stephanie M. Ribet,[1,a)] 🄸🄳 Georgios Varnavides,[1,2] 🄸🄳 Cassio C. S. Pedroso,[1] 🄸🄳 Bruce E. Cohen,[1] 🄸🄳
Peter Ercius,[1] 🄸🄳 Mary C. Scott,[1,3] 🄸🄳 and Colin Ophus[1,a)] 🄸🄳

AFFILIATIONS

[1]Molecular Foundry, Lawrence Berkeley National Laboratory, Berkeley, California 94720, USA
[2]Miller Institute for Basic Research in Science, University of California Berkeley, Berkeley, California 94720, USA
[3]Department of Materials Science and Engineering, University of California Berkeley, Berkeley, California 94720, USA

[a)]Authors to whom correspondence should be addressed: sribet@lbl.gov and cophus@gmail.com

ABSTRACT

In photon upconverting core–shell nanoparticles, structure strongly dictates performance. Typical imaging in scanning transmission electron microscopy has sufficient resolution to probe the atomic structure of these nanoparticles, but contrast, dose, and projection limitations make conventional methods insufficient for fully characterizing these structures. Phase retrieval techniques provide a promising alternative imaging mode, and, in particular, multislice electron ptychography can recover depth-dependent information. Here, we study beam-sensitive photon upconverting core–shell nanoparticles with a multislice ptychography approach using a low electron dose to avoid damage. Large strain fields arise in these heterostructures due to the mismatch in lattice parameter between the core and the shell. We reconstruct both a nanoparticle that appears defect-free and one that has a large break in the side and map the distribution of strain in 3D by computing distortion fields from high-resolution potential images of each slice. In the defect-free nanoparticle, we observe twisting of the shell, while in the broken nanoparticle, we measure the 3D position of the crack, the core, and dislocations. These results highlight the advantage of multislice electron ptychography to recover 3D information from a single scan, even under strict electron dose requirements from beam-sensitive samples.

Scanning transmission electron microscopy (STEM) imaging is a powerful tool to provide direct characterization of atomic-scale features in materials.[1] The small probe size of the converged beam allows for routine imaging of nanoscale defects.[2,3] Conventional bright- and dark-field STEM images are formed by collecting scattered electrons at a fixed angular range with monolithic integrating detectors. Despite the great success of these techniques in high-resolution characterization, conventional imaging modalities possess several limitations. STEM images are 2D projections of a 3D object, causing overlapping features to potentially be misinterpreted.[4] Bright- and dark-field imaging modalities are relatively dose inefficient, which limits their applicability for beam-sensitive materials.[5] Additionally, high angle annular dark-field (HAADF)-STEM, which is the most common STEM imaging configuration, has a nonlinear dependence on the atomic number of the species.[6] This composition-dependence leads to straightforward image interpretation, but dark-field imaging produces little to no contrast for low atomic number elements in most samples. For these reasons, there has been growing interest to develop STEM methods which overcome these limitations.[1]

Advances in hardware and software have led to the wide implementation of four dimensional (4D)-STEM techniques.[7] Instead of using conventional detectors, 4D-STEM experiments record full diffraction patterns at each probe position, which contain extensive structural information not accessible with conventional imaging modalities. Far-field pixelated detectors collect the intensity of the scattered wave, but the phase created by the interaction of the beam and sample is lost. Most of the information about the specimen is encoded in the phase of the electron exit wave, especially for weakly scattering samples. Techniques that recover the phase of the specimen provide dose-efficient characterization of weakly scattering materials, even in a matrix of heavy atoms.[8,9] There are a variety of TEM phase measurement methods including high-resolution transmission electron

11 July 2024 20:26:10

microscopy, holography, segmented-differential phase contrast, and 4D-STEM based approaches such as differential phase contrast, parallax, and ptychography.[8–14] Iterative electron ptychography algorithms, while more computationally demanding, are particularly powerful phase retrieval techniques. Ptychographic methods solve both the object and probe with a resolution limit set by the maximum scattering angle and allow for aberration correction in post-processing and super-resolution imaging.[9,15]

Multislice ptychography is beneficial for strongly scattering samples and allows for recovery of depth-dependent information.[16,17] In single slice ptychographic algorithms, the update for each iteration is calculated from a comparison with the experimental diffraction patterns and a projection computed by simple multiplication of the object and probe. As the object becomes more strongly scattering and the probe travels further through an object, this multiplicative assumption breaks down, leading to artifacts in the reconstruction. Instead, it is possible to replace the object with thin slices spatially separated along the beam direction [Fig. 1(a)].[9] In the forward projection, alternating transmission and free-space propagation steps are applied to each slice to account for changes with depth. For the backward update, the inverse operations are applied. When properly regularized and converged, multislice ptychography can partition the potential into slices corresponding to 3D information from the object. A variety of studies have demonstrated how scanning diffraction data encode depth information about a specimen, which can be reconstructed with post-processing.[18,19] Recent work and our simulations in the supplementary material have shown how multislice ptychography algorithms can make use of this depth information to characterize 3D structural features in a sample including defects.[17,20–23] These reconstructions have primarily explored single crystal samples using a high electron dose.

As a comparison, depth sectioning can also be performed with a series of images taken in conventional STEM modes at different defocus values. While more straightforward to implement, elongation artifacts can limit resolution along the direction of propagation of the beam, and these methods have the same dose and contrast challenges concomitant with STEM imaging.[24] Atomic electron tomography (AET) can provide full atomic resolution in all dimensions.[25] AET experiments use a series of images collected over many tilt projections, but these studies are generally limited to smaller volumes. Simultaneous imaging of heavy and light elements in 3D is possible with phase imaging approaches at each tilt.[26] These are technically more difficult experiments, especially under strict dose constraints, and they require much more computational power for reconstruction.[9,27]

Upconverting nanoparticles are Ln^{3+}-doped nanocrystals that convert infrared light to visible light and have significant interest for bioimaging,[28–30] optical materials,[31,32] and nanopatterning.[33] The addition of inert inorganic shells of Ln^{3+}-doped cores improves upconversion efficiency by 1–2 order of magnitude.[34,35] The dependence of performance on structure underscores the importance of characterizing these nanoparticles at high resolutions.

Core–shell $SrYbF_5$:1%Tm@CaF_2 particles are difficult to characterize with conventional imaging: these beam-sensitive upconverting nanoparticles damage under large doses, and the fluorine atomic constituents are challenging to image. Thus, we employed multislice ptychography to measure the structure of these core–shell nanoparticles. Details about the sample synthesis, experimental measurements, and reconstruction parameters are given in the supplementary material. We characterized the structure of two nanoparticles: one that appears pristine and one with a visible crack in the side [Figs. 1(b) and 1(c)]. Because we have reconstructed the atomic potential with depth resolution, we are able to map the depth-dependent strain fields and defect positions. This work demonstrates the dose-efficient nature of multislice ptychography and extends this approach to strain and defect mapping of larger, complex material systems.

A HAADF-STEM image of the $SrYbF_5$:1%Tm@CaF_2 core–shell nanoparticle is shown in Fig. 1(b), and more images are shown in Fig. S1 and in prior work.[36] The compositional contrast of the dark-field image makes it straightforward to distinguish between the core and the shell. These nanoparticles have an approximate shell thickness of 3.5 nm, although as shown in Fig. 1(b), the core can be off-center. It is not possible to observe the fluorine atoms in the dark-field image. Most of the particles were intact, but in some cases, we observed splitting of the shell, as shown in Fig. 1(c) and Fig. S1(b). We hypothesize that these cracks form in response to the large strain fields caused by the difference in lattice parameter between the core and the shell. Both $SrYbF_5$ and CaF_2 have a cubic structure. $SrYbF_5$ has a unit cell side length of 5.7 Å, while CaF_2 has a unit cell dimension of 5.5 Å.[28]

We characterized the nanoparticle shown in Fig. 1(b) using a gradient descent multislice approach implemented in the open-source `py4DSTEM` toolkit.[9,37] We constrain the object to be a positive potential object, and slices from a top, middle, and bottom are shown in Fig. 2, with all 1.2 nm slices shown in Fig. S2. Given the low electron dose (5×10^3 e$^-$/Å^2) demanded by these beam-sensitive structures, additional regularization was applied on the probe and object to help with convergence, with details provided in the supplementary material. The ptychographic reconstructions reveal the structure more clearly as the fluorine atoms become visible (Fig. S3). Depth-dependent information shows that the particle is more complex than previously understood from dark-field imaging. The contrast in the reconstructed potential is sensitive to tilt. Areas where the lattice is aligned with the electron beam, such that the specimen is on zone, appear bright, while tilted regions appear dim. The multislice reconstruction uncovers that
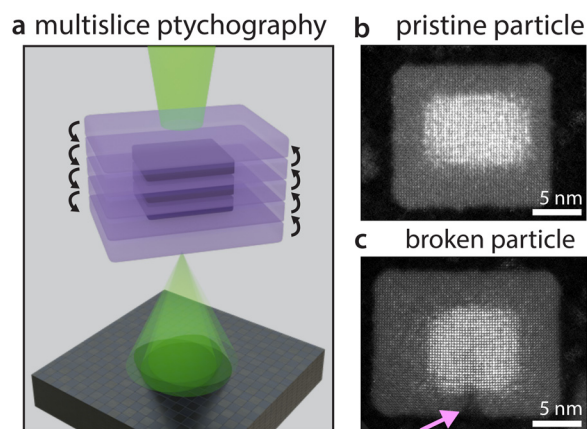

FIG. 1. (a) Geometry of a multislice ptychographic reconstruction using a defocused electron probe, where the sample is broken into slices along the beam direction. Arrows show forward and backward propagation during multislice reconstruction. HAADF-STEM imaging of (b) a pristine $SrYbF_5$:1%Tm@CaF_2 nanoparticle and (c) a nanoparticle containing a large crack at the bottom indicated by arrow.
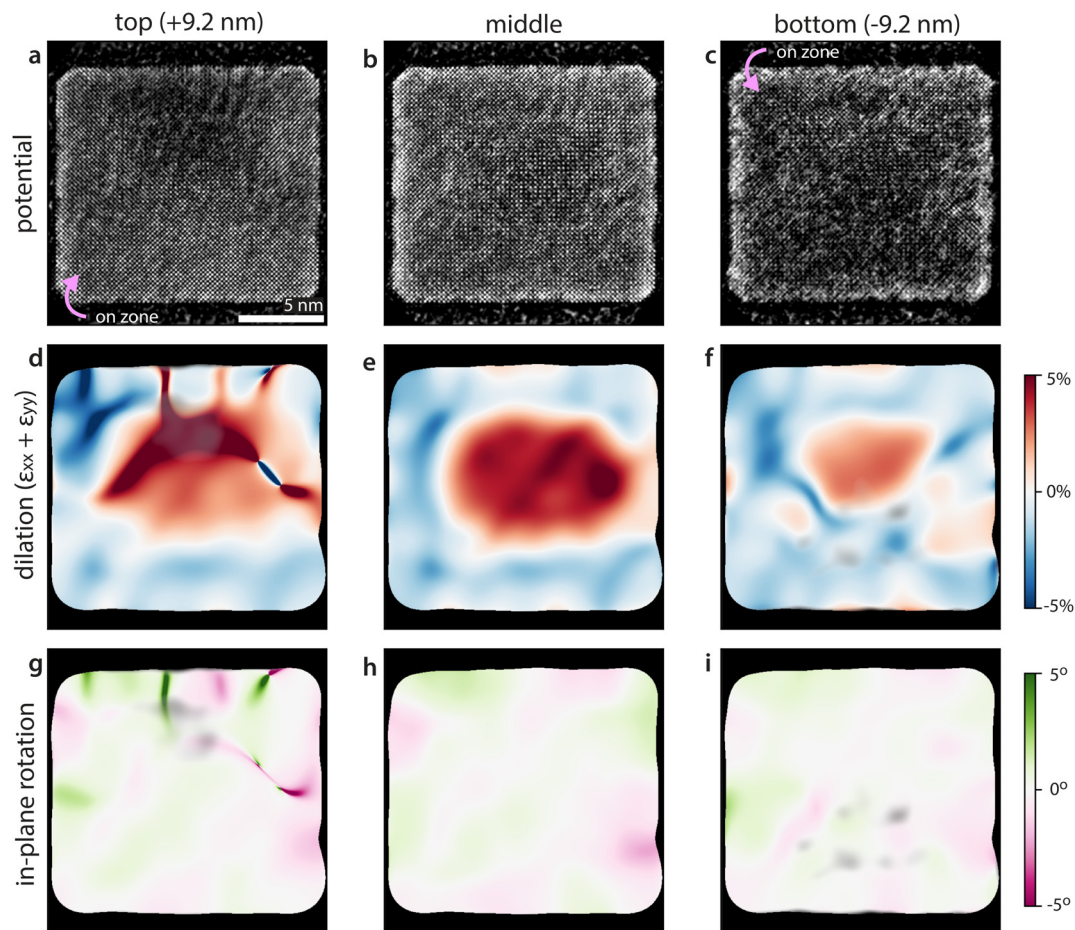
FIG. 2. (a)–(c) Top, middle, and bottom slice reconstruction of core–shell nanoparticle in Fig. 1(b), and their corresponding masked (d)–(f) dilation and (g)–(i) rotation maps.

the tilting of the nanoparticle changes with depth, suggesting twisting, especially of the shell. In Fig. 2(a), a slice from the top of the particle, the center, and bottom portion of the particle is on zone. However, a slice from further down the nanoparticle [Fig. 2(c)] shows the area in the opposite corner is on zone, as indicated by the arrows.

We have calculated maps of the sample strain using geometric phase analysis (GPA) of each slice of the reconstruction.[38] More details about strain and structural analysis can be found in the supplementary material. Figures 2(d)–2(f) show the strain dilation (sum of in-plane strain in both directions) from these slices and the corresponding in-plane rotation [Figs. 2(g)–2(i)] from the strain tensor. The dominant feature in these images is the large dilation due to the lattice mismatch between the core and the shell. Additional strain accumulation at the interface between the core and the shell and dipoles are present in the top slice indicating more defects near the top.

The strain maps were masked in real space based on the magnitude of the Fourier components used for the strain analysis as shown in Fig. S4. Because GPA uses a finite mask around each Bragg peak considered, it has a non-zero "kernel size" in real space and will produce strain measurements dilated by the size of this kernel. While we attempted to determine an accurate mask for the strain maps in an unbiased manner, noise in the low spatial frequency components could distort the mask edges. Moreover, the mask uses a sharp cutoff instead of a soft edge, so by nature, the strain profiles are more reliable away from the edge of the particle. For example, the dipoles at the edge of Fig. 2(d), especially in the upper right corner, may indicate a dislocation or an artifact from the strain mapping.

We apply a similar analysis approach to the broken particle, as shown in Fig. 1(c), and the results are shown in Fig. 3 with all slices shown in Fig. S5. In this case, we do not observe as much tilting of the particle, but instead see the evolution of the crack morphology as a function of depth. In particular, the depth-dependent contrast suggests that the crack is growing toward the top of the particle. This feature is also reflected in the rotation maps. The magnitude of the rotation in the top slice [Fig. 3(g)] is much larger than in the middle [Fig. 3(h)] or bottom [Fig. 3(i)], suggesting the particle is being pulled apart as the crack expands. The dilation maps also show multiple strain dipoles corresponding to lattice dislocations and more compressive strain near the break.

To better understand the architecture of the broken particle, we estimated its 3D structure. Figure 4(a) shows the surface of the particle, which was calculated using the magnitude of the Fourier peaks from
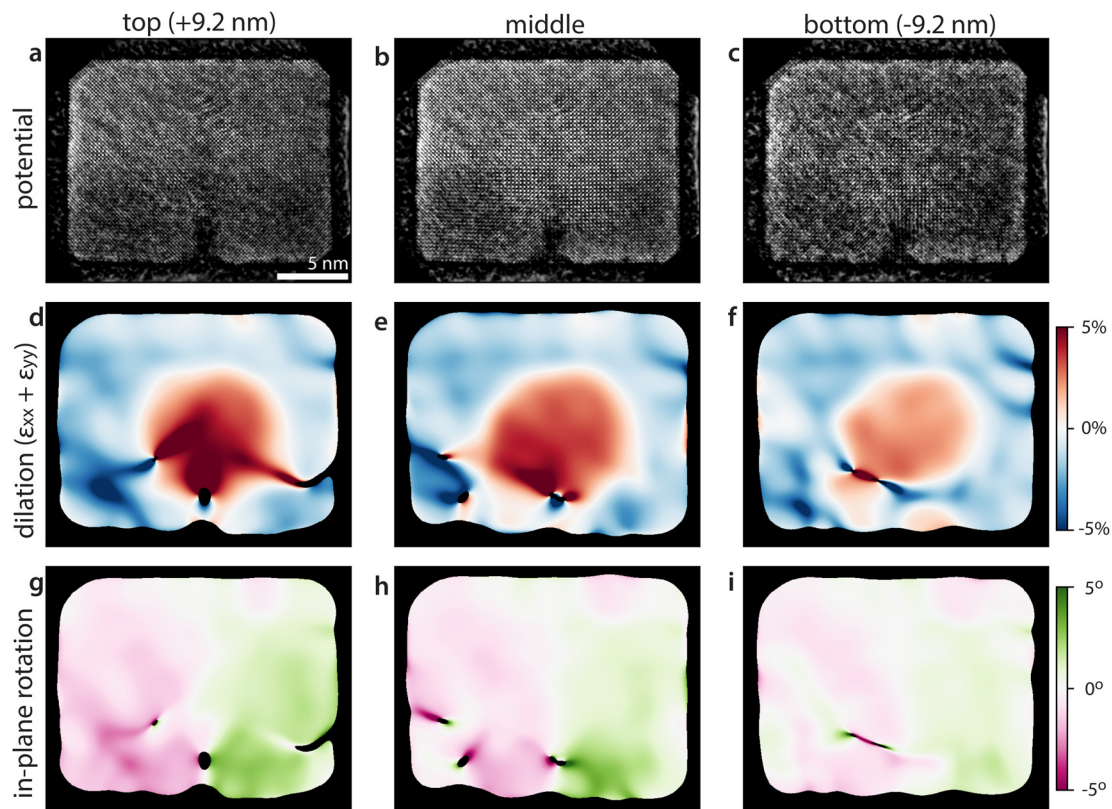
FIG. 3. (a)–(c) Top, middle, and bottom slice reconstruction of core–shell nanoparticle in Fig. 1(c), and their corresponding masked (d)–(f) dilation and (g)–(i) rotation maps.
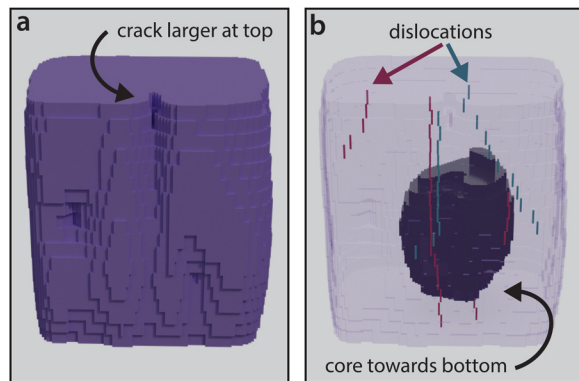

FIG. 4. (a) Surface of particle in Fig. 3 estimated from particle edge in potential sli-ces. (b) Internal structure shows shell (purple) and core position (black) and disloca-tions (in blue and red).

the lattice. In agreement with the rotation maps in Fig. 3, the crack is largest toward the top of the particle. We can probe the location of the core relative to the shell by measuring an order parameter correspond-ing to the relative intensities of the two sublattices with different com-positions (measured from the Bragg peak intensities of the image Fourier transforms), which is shown in Fig. S6. From this analysis, we

find the core is also off-center along the beam direction, positioned closer to the bottom of the particle. Finally, we can also plot the posi-tion of dislocations with in-plane Burger vectors in each slice (Fig. S7). We use Bragg filtering on two of the lattice peaks as indicated in Fig. S8 to plot the dislocation positions in each slice [Fig. 4(b)]. We find dislocations forming toward the edge or interface between the core and shell in the nanoparticle, with some traveling through the full depth.

Work with upconverting nanoparticles which are exceptionally sensitive to changes in quenching[33] has shown that defects at the core/ shell interface underlie photoswitching,[33] and that minor variations in shell thickness can mediate large changes in upconversion efficiency,[34] although the origins of both effects are poorly understood.[34] The methods described here for characterizing the core–shell interface offer a promising route for exploring mechanisms that arise from interfacial strain or structural defects.

This work highlights both the limitations and benefits of multi-slice ptychography. Ptychographic reconstructions require solving high-dimensional, non-convex, inverse scattering problems, which becomes additionally difficult with experimental artifacts such as probe position jitter and sample limitations such as electron dose constraints. It can be a challenge to converge low spatial frequency features for iter-ative ptychographic methods when using a large convergence angles, especially at low electron doses.[9,39] Our reconstructions are susceptible to these artifacts, such as the extra intensity at the edge of the particle

as shown in Figs. S2 and S5. These intensity fluctuations could create spurious strain artifacts, such as some of the strain features on the edges of particles in Figs. 2 and 3. Here, we converge the normalized mean squared error to ensure internal self-consistency and employ regularization constraints on the reconstructed probe and object to reduce the available solution phase-space and arrive at a physical solution. While the algorithms converge to a feasible solution, there are no formal guarantees this will be the optimal solution.

The maximal achievable resolution along the beam direction in multislice ptychography is currently limited to the nanometer scale,[17] and in this study, the resolution is approximately 3.8 nm (Fig. S9). Therefore, additional caution should be exercised in interpreting features in a single 1.2 nm slice, as compared to trends which extend between slices. Figure 4, for example, shows dislocations which traverse many slices giving additional credence to their interpretation. Features tend to get more blurred out and lengthened along the direction of travel of the electron beam. This artifact makes quantification of the absolute aspect ratio and of the termination of top and bottom surfaces challenging without additional information. Both a larger convergence angle and a higher electron dose would better resolve out-of-plane features. Collecting additional scans at other tilt angles would be especially valuable to provide information about the changing morphology of the particle along the direction of propagation of the beam. Because of the limited depth resolution of this study, we can only measure the in-plane components of the strain tensor, though we have demonstrated the depth-dependence of these deformations.

Despite these limitations, this work demonstrates how multislice ptychography can resolve out-of-plane structural features from a single scan at relatively low dose. Our simulations shown in Figs. S10 and S11 highlight the effectiveness of multislice ptychography in reconstructing the changing morphology of a structure with depth. We show dislocations traversing the depth of a particle. With multislice simulations at conditions that match our experimental parameters, we are able to recover the positions of the defects and resulting strain fields. While real world samples are more complex as they contain multiple dislocations, tilt, and cracks, these computations emphasize the power of multislice ptychography to recover small changes in materials along the direction of propagation of the beam. Moreover, our own experimental work with a challenging sample highlights how multislice ptychography lends itself to the characterization of large, heterostructures and defects in materials, suggesting the broader applications of this technique in materials science and engineering.

See the supplementary material for methods details, supporting figures, and videos showing all the slices from the reconstructions.

AUTHOR DECLARATIONS

Conflict of Interest

The authors have no conflicts to disclose.

Author Contributions

Stephanie M. Ribet: Conceptualization (equal); Formal analysis (equal); Investigation (equal); Methodology (equal); Software (equal); Writing – original draft (equal); Writing – review & editing (equal). **Georgios Varnavides:** Methodology (equal); Software (equal); Writing – review & editing (equal). **Cassio C. S. Pedroso:** Investigation (equal); Writing – review & editing (equal). **Bruce E. Cohen:** Resources (equal); Supervision (equal); Writing – review & editing (equal). **Peter Ercius:** Resources (equal); Writing – review & editing (equal). **Mary C. Scott:** Resources (equal); Writing – review & editing (equal). **Colin Ophus:** Conceptualization (equal); Formal analysis (equal); Methodology (equal); Resources (equal); Software (equal); Supervision (equal); Writing – review & editing (equal).

DATA AVAILABILITY

The data that support the findings of this study are openly available in Zenodo at https://zenodo.org/records/10775819, Ref. 40.

REFERENCES

[1]C. Ophus, "Quantitative scanning transmission electron microscopy for materials science: Imaging, diffraction, spectroscopy, and tomography," Annu. Rev. Mater. Res. **53**, 105 (2023).

[2]O. L. Krivanek, M. F. Chisholm, V. Nicolosi, T. J. Pennycook, G. J. Corbin, N. Dellby, M. F. Murfitt, C. S. Own, Z. S. Szilagyi, M. P. Oxley *et al.*, "Atom-by-atom structural and chemical analysis by annular dark-field electron microscopy," Nature **464**, 571–574 (2010).

[3]P. J. Phillips, M. De Graef, L. Kovarik, A. Agrawal, W. Windl, and M. Mills, "Atomic-resolution defect contrast in low angle annular dark-field stem," Ultramicroscopy **116**, 47–55 (2012).

[4]P. A. Midgley and R. E. Dunin-Borkowski, "Electron tomography and holography in materials science," Nat. Mater. **8**, 271–280 (2009).

[5]Q. Chen, C. Dwyer, G. Sheng, C. Zhu, X. Li, C. Zheng, and Y. Zhu, "Imaging beam-sensitive materials by electron microscopy," Adv. Mater. **32**, 1907619 (2020).

[6]M. M. Treacy, "Z dependence of electron scattering by single atoms into annular dark-field detectors," Microsc. Microanal. **17**, 847–858 (2011).

[7]C. Ophus, "Four-dimensional scanning transmission electron microscopy (4D-STEM): From scanning nanodiffraction to ptychography and beyond," Microsc. Microanal. **25**, 563–582 (2019).

[8]H. Rose, "Nonstandard imaging methods in electron microscopy," Ultramicroscopy **2**, 251–267 (1976).

[9]G. Varnavides, S. M. Ribet, S. E. Zeltmann, Y. Yu, B. H. Savitzky, V. P. Dravid, M. C. Scott, and C. Ophus, "Iterative phase retrieval algorithms for scanning transmission electron microscopy," arXiv:2309.05250 (2023).

[10]R. Close, Z. Chen, N. Shibata, and S. Findlay, "Towards quantitative, atomic-resolution reconstruction of the electrostatic potential via differential phase contrast using electrons," Ultramicroscopy **159**, 124–137 (2015).

[11]C. Ophus, J. Ciston, J. Pierce, T. R. Harvey, J. Chess, B. J. McMorran, C. Czarnik, H. H. Rose, and P. Ercius, "Efficient linear phase contrast in scanning transmission electron microscopy with matched illumination and detector interferometry," Nat. Commun. **7**, 10719 (2016).

[12]H. Yang, P. Ercius, P. D. Nellist, and C. Ophus, "Enhanced phase contrast transfer using ptychography combined with a pre-specimen phase plate in a scanning transmission electron microscope," Ultramicroscopy **171**, 117–125 (2016).

[13]J. Rodenburg and A. Maiden, "Ptychography," in *Springer Handbook of Microscopy* (Springer Nature, 2019), pp. 819–904.

[14]R. E. Dunin-Borkowski, A. Kovács, T. Kasama, M. R. McCartney, and D. J. Smith, "Electron holography," in *Springer Handbook of Microscopy* (Springer Nature, 2019), pp. 767–818.

[15]Y. Jiang, Z. Chen, Y. Han, P. Deb, H. Gao, S. Xie, P. Purohit, M. W. Tate, J. Park, S. M. Gruner *et al.*, "Electron ptychography of 2D materials to deep sub-ångström resolution," Nature **559**, 343–349 (2018).

[16]A. M. Maiden, M. J. Humphry, and J. M. Rodenburg, "Ptychographic transmission microscopy in three dimensions using a multi-slice approach," J. Opt. Soc. Am. A **29**, 1606–1614 (2012).

[17]Z. Chen, Y. Jiang, Y.-T. Shao, M. E. Holtz, M. Odstrčil, M. Guizar-Sicairos, I. Hanke, S. Ganschow, D. G. Schlom, and D. A. Muller, "Electron ptychography achieves atomic-resolution limits set by lattice vibrations," Science **372**, 826–831 (2021).

[18]S. Gao, P. Wang, F. Zhang, G. T. Martinez, P. D. Nellist, X. Pan, and A. I. Kirkland, "Electron ptychographic microscopy for three-dimensional imaging," Nat. Commun. **8**, 163 (2017).

[19]C. Ophus, T. R. Harvey, F. S. Yasin, H. G. Brown, P. M. Pelz, B. H. Savitzky, J. Ciston, and B. J. McMorran, "Advanced phase reconstruction methods enabled by four-dimensional scanning transmission electron microscopy," Microsc. Microanal. **25**, 10–11 (2019).

[20]Z. Dong, M. Huo, J. Li, J. Li, P. Li, H. Sun, Y. Lu, M. Wang, Y. Wang, and Z. Chen, "Visualization of oxygen vacancies and self-doped ligand holes in La$_3$Ni$_2$O$_{7-\delta}$," arXiv:2312.15727 (2023).

[21]D. Yoon, Y.-T. Shao, Y. Yang, D. Ren, H. D. Abruña, and D. A. Muller, "Imaging Li vacancies in a Li-ion battery cathode material by depth sectioning multi-slice electron ptychographic reconstructions," Microsc. Microanal. **29**, 1263–1264 (2023).

[22]X. Chen, C. Gilgenbach, and J. M. LeBeau, "Characterization of quantum emitters and extended defects in ZnSe via multislice electron ptychography," Microsc. Microanal. **29**(Supplement_1), 342–343 (2023).

[23]C. Gilgenbach, X. Chen, M. Xu, and J. LeBeau, "Three-dimensional analysis of nanoscale dislocation loops with multislice electron ptychography," Microsc. Microanal. **29**(Supplement_1), 286–287 (2023).

[24]H. L. Xin and D. A. Muller, "Aberration-corrected ADF-STEM depth sectioning and prospects for reliable 3D imaging in S/TEM," Microscopy **58**, 157–165 (2009).

[25]J. Miao, P. Ercius, and S. J. Billinge, "Atomic electron tomography: 3D structures without crystals," Science **353**, aaf2157 (2016).

[26]P. M. Pelz, S. M. Griffin, S. Stonemeyer, D. Popple, H. DeVyldere, P. Ercius, A. Zettl, M. C. Scott, and C. Ophus, "Solving complex nanostructures with ptychographic atomic electron tomography," Nat. Commun. **14**, 7906 (2023).

[27]J. Lee, M. Lee, Y. Park, C. Ophus, and Y. Yang, "Multislice electron tomography using four-dimensional scanning transmission electron microscopy," Phys. Rev. Appl. **19**, 054062 (2023).

[28]S. Fischer, C. Siefe, D. F. Swearer, C. A. McLellan, A. P. Alivisatos, and J. A. Dionne, "Bright infrared-to-ultraviolet/visible upconversion in small alkaline earth-based nanoparticles with biocompatible CaF$_2$ shells," Angew. Chem. Int. Ed. **59**, 21603–21612 (2020).

[29]C. C. Pedroso, V. R. Mann, K. Zuberbühler, M.-F. Bohn, J. Yu, V. Altoe, C. S. Craik, and B. E. Cohen, "Immunotargeting of nanocrystals by spycatcher conjugation of engineered antibodies," ACS Nano **15**, 18374–18384 (2021).

[30]H. Najafiaghdam, C. C. Pedroso, N. A. Torquato, B. E. Cohen, and M. Anwar, "Fully integrated ultra-thin intraoperative micro-imager for cancer detection using upconverting nanoparticles," Mol. Imaging Biol. **25**, 168–179 (2023).

[31]V. R. Mann, F. Manea, N. J. Borys, C. M. Ajo-Franklin, and B. E. Cohen, "Controlled and stable patterning of diverse inorganic nanocrystals on crystalline two-dimensional protein arrays," Biochemistry **60**, 1063–1074 (2021).

[32]A. Fernandez-Bravo, K. Yao, E. S. Barnard, N. J. Borys, E. S. Levy, B. Tian, C. A. Tajon, L. Moretti, M. V. Altoe, S. Aloni *et al.*, "Continuous-wave upconverting nanoparticle microlasers," Nat. Nanotechnol. **13**, 572–577 (2018).

[33]C. Lee, E. Z. Xu, K. W. Kwock, A. Teitelboim, Y. Liu, H. S. Park, B. Ursprung, M. E. Ziffer, Y. Karube, N. Fardian-Melamed *et al.*, "Indefinite and bidirectional near-infrared nanocrystal photoswitching," Nature **618**, 951–958 (2023).

[34]K. W. Kwock, C. Lee, A. Teitelboim, Y. Liu, K. Yao, S. B. Alam, B. E. Cohen, E. M. Chan, and P. J. Schuck, "Surface-sensitive photon avalanche behavior revealed by single-avalanching-nanoparticle imaging," J. Phys. Chem. C **125**, 23976–23982 (2021).

[35]B. Tian, A. Fernandez-Bravo, H. Najafiaghdam, N. A. Torquato, M. V. P. Altoe, A. Teitelboim, C. A. Tajon, Y. Tian, N. J. Borys, E. S. Barnard *et al.*, "Low irradiance multiphoton imaging with alloyed lanthanide nanocrystals," Nat. Commun. **9**, 3082 (2018).

[36]A. Pattison, C. Pedroso, B. E. Cohen, W. Theis, and P. Ercius, "Advanced techniques in automated high resolution scanning transmission electron microscopy," Nanotechnology **35**, 015710 (2024).

[37]B. H. Savitzky, S. E. Zeltmann, L. A. Hughes, H. G. Brown, S. Zhao, P. M. Pelz, T. C. Pekin, E. S. Barnard, J. Donohue, L. R. DaCosta *et al.*, "py4DSTEM: A software package for four-dimensional scanning transmission electron microscopy data analysis," Microsc. Microanal. **27**, 712–743 (2021).

[38]M. J. Hÿtch, E. Snoeck, and R. Kilaas, "Quantitative measurement of displacement and strain fields from HREM micrographs," Ultramicroscopy **74**, 131–146 (1998).

[39]L. Zhou, J. Song, J. S. Kim, X. Pei, C. Huang, M. Boyce, L. Mendonça, D. Clare, A. Siebert, C. S. Allen *et al.*, "Low-dose phase retrieval of biological specimens using cryo-electron ptychography," Nat. Commun. **11**, 2773 (2020).

[40]S. M. Ribet *et al.*, "Uncovering the three-dimensional structure of upconverting core-shell nanoparticles with multislice electron ptychography," Zenodo. https://zenodo.org/records/10775819

11 July 2024 20:26:10